PHYSICAL REVIEW E **89**, 023105 (2014)

Evolution of frequency clusters in the naturally occurring dust acoustic wave

J. D. Williams[*]

Department of Physics, Wittenberg University, Springfield, Ohio 45504, USA

(Received 3 January 2014; published 18 February 2014)

The spatiotemporal evolution of the naturally occurring dust acoustic wave mode is experimentally investigated in a weakly coupled dc glow discharge dusty plasma system over a range of neutral gas pressures through the application of a time-resolved Hilbert Transform. Frequency clusters are observed over a range of neutral gas pressures, though their spatial distribution varies with neutral gas pressure. It is also observed that the wave frequency is observed to drop by ∼10 Hz across these frequency clusters independent of the experimental parameters.

DOI: 10.1103/PhysRevE.89.023105 PACS number(s): 52.27.Lw, 52.27.Gr

I. INTRODUCTION

A dusty (complex) plasma is a four-component plasma system that is composed of ions, electrons, neutral particles, and charged microscopic particles or "dust." The dust, which in the laboratory setting typically consists of nanometer- to micrometer-sized particles, becomes charged through interactions with the background plasma, which leads to the dust entering into the plasma system. Once in the plasma system, the dust interacts with and self-consistently modifies the properties of the surrounding plasma medium. The result is a system that is significantly more complex than the traditional three-component plasma and supports a range of new plasma phenomena [1–5], including a collective mode known as the dust acoustic wave (also known as the dust density wave) [6–11]. This low-frequency longitudinal mode propagates through the dust component and is self-excited by the free energy from the ion streaming through the dust component [12].

Over the past 20 years, the linear and nonlinear properties of the dust acoustic wave have been the subject of intense theoretical and experimental study owing, in part, to the fact that the relatively large particle size of the dust allows for direct visual observation at the kinetic level while the low charge-to-mass ratio of the dust results in a system whose characteristic frequencies (∼Hz) allow for the use of diagnostic tools as simple as a video imaging. Among the topics that have been recently studied are wave-particle interaction [13–15], the growth [16–19] and dispersion relation [20–25] of this wave mode, wave breaking [26,27], shocks [28,29], synchronization [20–23,25,30–33], and turbulence [34,35]. Recently, the application of the Hilbert transform technique to experimental data taken under microgravity conditions in a radio-frequency discharge plasma revealed that the wave field exhibits distinct regions of constant and different frequencies known as frequency clusters [32,36]. The observation of frequency clusters was subsequently observed when numerically simulating the system as an ensemble of mutually coupled nonlinear van der Pol oscillators [37].

In the following paper, we apply a time-resolved Hilbert transform to high-speed imaging of the naturally occurring dust acoustic wave in a dc glow discharge plasma and report on the evolution of the spatial distribution of frequencies in this wave mode. Section II describes the experimental setup and methods, followed by a presentation of the experimental observations in Sec. III. A final summary and conclusions are presented in Sec. IV.

II. EXPERIMENTS AND ANALYSIS

A. Experimental setup and procedure

The experiments presented here were performed in the Wittenberg University DUsty Plasma DEvice (WUDUPE) [38]. A side view of the experimental setup is seen in Fig. 1. In this device, an argon plasma is generated by biasing a 2.54-cm-diameter (1 in.) brass electrode positive with respect to the grounded vacuum chamber wall using a voltage controlled, constant current power supply at fixed dc currents from ∼0.15–0.3 mA with bias voltages of ∼300 V.

Dust particles are introduced into the plasma from an electrically floating 2.54-cm-diameter electrode, loaded with 1.98-μm-diameter melamine microspheres ($\rho = 1510\,\mathrm{kg/m^3}$), positioned approximately 7.5 cm below the anode. Once the plasma has been ignited, these particles acquire a net negative charge from the background plasma and are lifted from the tray into the discharge over a period of several minutes, after which a stable dust cloud is observed to be suspended in the anode glow of the discharge where the dust is confined by the gravitational force and the electric force due to the self-consistently formed potential structure of the anode.

Once a dust cloud has formed, the experimental conditions are adjusted until a self-excited dust acoustic wave is observed to spontaneously appear and propagate in the y direction, i.e., parallel to the direction of gravity. It is noted that this wave mode can only be observed when the energy gain from the ions exceeds the energy loss through collisions with neutral particles [12]. As a result, the experiments presented here were performed over a range of neural gas pressures from 91 to 118 mTorr.

The plasma parameters were measured when no dust was present using a double probe and were found to constant over the range of neutral gas pressures examined, with $n_e \sim 10^{13}$ m^{-3} and $T_e \sim$ 5–8 eV. From the images acquired, the number density of the dust component was found to be $n_d \sim 10^9$–10^{10} m^{-3}. The dust charge can be estimated using OML theory and is calculated to be ∼5400 electron

---

[*] jwilliams@wittenberg.edu

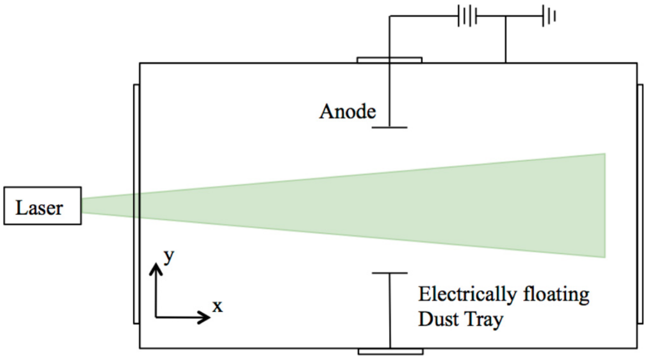

FIG. 1. (Color online) Sketch of the experimental apparatus. The dust clouds examined here form between the anode and the electrically floating dust tray.

charges. It is noted that this calculation overestimates the actual dust charge as OML theory neglects collisional [39] and ionization [40] enhancements due to the ion collection. The reader is referred to Ref. [19] for a more complete description of the experimental parameters.

To observe the dynamics of this wave mode, the dust particles are illuminated using a 200-mW diode-pumped solid-state laser ($\lambda = 532$ nm) whose output was expanded into a 2-mm-thick vertical light sheet and imaged using a Photron SA3 CMOS camera that is positioned perpendicular to the laser sheet. The camera was equipped with a band-pass filter to eliminate light emitted by the background plasma glow and video sequences consisting of 1000 images were acquired at a rate of 250 fps. It is noted that this camera has a linear response to light, which allows the intensity in the recorded images to be used as a surrogate for the number density of the dust component.

B. Wave properties

A representative image of a dust cloud examined here, recorded at $p = 91$ mTorr and $I_{\text{dis}} = 0.2$ mA, is seen in Fig. 2(a) and depicts the spatial properties of the natural wave mode as it propagates away from the anode (located at $y > 0$ mm) in the direction of gravity (decreasing y). It is observed that the wavelength increases as the wave propagates through the background dust cloud. The wavelengths in the upper ($-10 \leqslant y \leqslant -35$ mm) and lower regions ($-40 \leqslant y \leqslant -65$ mm) of the cloud for the different neutral gas pressures examined here are summarized in Table I. It is also observed that the wavefronts are not strictly parallel to each other, particularly at lower pressures, and there are several instances of dislocations (defects) in wavefront where individual wavefronts are observed to merge or split. These bifurcations in the wavefront, seen in Fig. 2(a), are the result of different regions of an individual wavefront traveling with different phase velocities. This results in the defect moving along the wavefront and either splitting off of the initial wavefront to form a new wavefront or merging with another wavefront in a zipper-like fashion. Further, there are instances where all regions of an individual wavefront are observed to travel at the same speed but overtake another wavefront that is traveling at a slower speed. Both behaviors are observed at each of the neutral gas pressures examined here and have been observed in other experiments [23,29,37]. These bifurcations in the wavefront indicate regions where wavefronts are added or removed from the system, suggesting the possibility of a topological defect and the existence of frequency clusters [32,36].

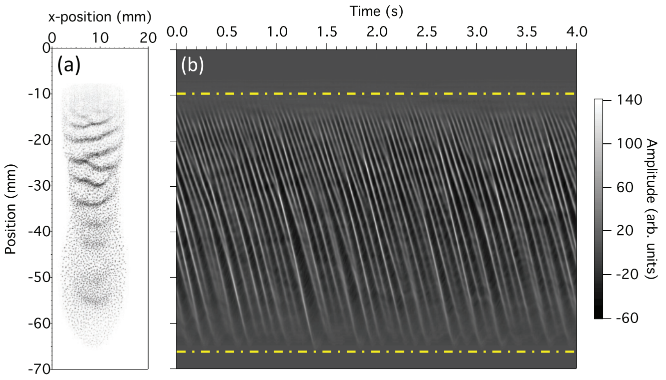

FIG. 2. (Color online) (a) An inverted image of a dust cloud at $p = 91$ mTorr. (b) A space-time diagram constructed from intensity profiles extracted at $x = 9$ mm in the image seen in (a). The light bands denote the propagation of individual wavefronts through the dust cloud. The (yellow) dashed-dot lines indicate the top and bottom of the dust cloud.

TABLE I. Comparison of wave properties in the upper and lower regions of the dust clouds.

Region	p (mTorr)	f (Hz)	λ (mm)	v_{ph} (mm/s)
Upper	91	1.8 ± 0.3	21 ± 3	67 ± 8
	102	1.8 ± 0.2	19 ± 2	67 ± 5
	118	2.6 ± 0.6	20 ± 7	56 ± 9
Lower	91	6.1 ± 1.9	11 ± 3	92 ± 8
	102	6.9 ± 2.0	10 ± 3	80 ± 8
	118	6.8 ± 1.5	10 ± 2	77 ± 2

The temporal properties of the wave seen in Fig. 2(a) can be seen in the space-time plot in Fig. 2(b). Here, each vertical line represents an intensity profile from the center of the imaged dust cloud at $x = 9$ mm in Fig. 2(a). In this plot, the downward sloping bands depict the propagation of individual wavefronts and the slope of each band depicts the phase velocity of that wavefront. The variation that is observed in the slope of these bands as each individual wavefront propagates from the top to the bottom of the dust cloud indicates that the phase velocity increases as the wave propagates through the dust cloud. This variation in the phase velocity results in the merging or splitting of wavefronts previously described and is seen as either the merging of two (or more) of these sloping bands or as the splitting of one of the sloping bands seen in Fig. 2(b). Here, it is clearly seen that wavenumber is not conserved as wavefronts are either added or removed from the system at these bifurcation points. The phase velocities in the upper and lower regions of the cloud for the different neutral gas pressures examined here are summarized in Table I. Finally, the variation in the horizontal spacing of the sloping bands that is seen when comparing the upper and lower regions of the dust clouds indicates that the frequency decreases as the wave propagates through the cloud. The average frequencies from the upper and lower regions of the cloud are also summarized in Table I.

Taken together, these results indicate the dust acoustic waves examined here are nonlinear, a result that is consistent with previous studies of dust clouds under these experimental conditions [19].

C. Data analysis

Given the variation in the spatiotemporal properties of the wave mode seen in Fig. 2 and Table I, a measure of the spatiotemporal evolution of the wave properties is necessary to obtain a more complete understanding of this wave mode. To do this, we compute the temporal evolution of the frequency at each spatial location using the analytic signal that is constructed from the wave structure by following the general process described by Menzel *et al.* [32,36]. The key steps are detailed below.

The wave structure at each pixel location as a function of time, $n_d(x, y, t)$, is found by applying a Gaussian low-pass filter to each image to suppress the effects of the granularity of individual particles and then subtracting the time-averaged background dust density from each filtered image. An example of the density fluctuations associated with this wave mode at a single spatial (pixel) location is seen in Fig. 3(a).

The analytic signal, $A(x, y, t)$, is then constructed by expanding the measured wave structure, $n_d(x, y, t)$, into the complex plane according to Eq. (1),

$$\begin{aligned} A(x,y,t) &= n_d(x,y,t) + \imath \hat{n}_d(x,y,t) \\ &= E(x,y,t)\exp[i\phi(x,y,t)], \end{aligned} \tag{1}$$

where $\hat{n}_d(x,y,t)$ is the Hilbert Transform of the measured wave structure, $n_d(x, y, t)$, $E(x, y, t) = (n_d^2 + \hat{n}_d^2)^{1/2}$ is the envelope function, and $\phi(x,y,t) = \mathrm{atan2}[\hat{n}_d(x,y,t), n_d(x,y,t)]$ is the instantaneous phase. The instantaneous phase is then unwrapped to eliminate discontinuities due to phase jumps from $2\pi \to 0$. The unwrapped instantaneous phase that is calculated from the density fluctuations depicted in Fig. 3(a) is seen in Fig. 3(b), while the envelope function is depicted by the dashed (blue) line in Fig. 3(a). From this, the instantaneous frequency, $f_i(t_o)$, can be found from the temporal derivative of the instantaneous phase.

$$f_i(t_o) = \frac{1}{2\pi} \cdot \left.\frac{\partial\phi(t)}{\partial t}\right|_{t=t_o} \tag{2}$$

The monotonically increasing nature of the instantaneous phase allows the signal to noise ratio to be improved by averaging over several values of the instantaneous frequency, $f_m = \langle f_i(t)\rangle_{\Delta t}$. In earlier work [32,36], the mean frequency, f_m, was found by averaging over tens of periods. In this analysis, a smaller value of $\Delta t = 136$ ms was used to provide temporal resolution of the frequency while optimizing the signal-to-noise ratio. The choice of Δt used here corresponds to averaging over two wave periods for a wave at 15 Hz, a value that is typical in this device under the experimental conditions examined. This time-averaged, or mean, frequency is superimposed on a periodogram that is constructed by performing a short-time Fourier transform on the measured wave structure in Fig. 3(c).

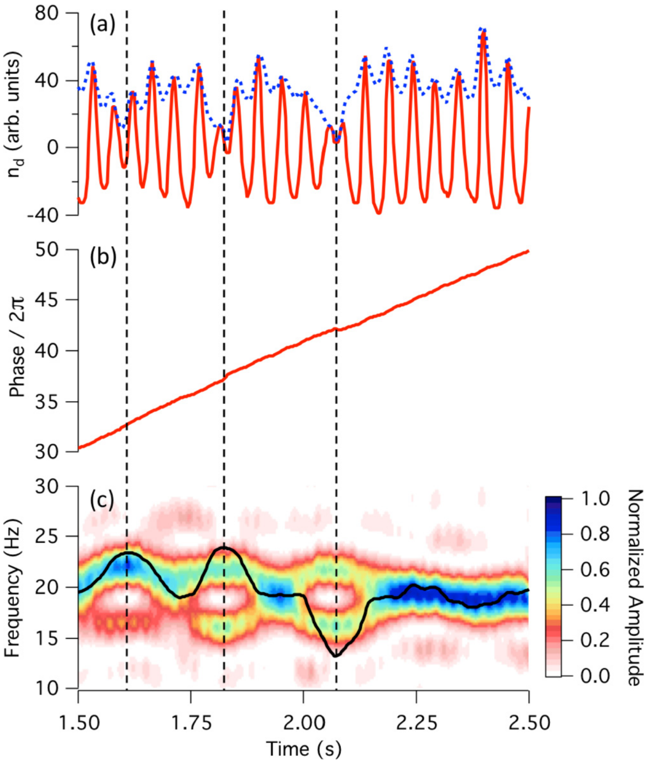

FIG. 3. (Color online) (a) Plot of the wave structure at a single pixel location as a function of time (solid, red curve). The dashed (blue) curve denotes the envelope function. (b) Plot of the unwrapped phase as a function of time at the same pixel location. (c) Plot of the mean frequency (solid, black curve) as a function of time superimposed on a periodogram constructed by applying a short-time Fourier Transform to the measured wave structure. The sudden variations that are observed in the mean frequency occur when bifurcations are observed on the wave structure and are correlated with discontinuities in the unwrapped phase and sudden decreases in the wave amplitude, suggesting the existence of a topological defect.

Over the period of data examined here, there are two distinct regions, an initial period ($1.5 < t < 2.2$ s), where there is significant variation in the frequency, followed by a period ($2.2 < t < 2.5$ s), where only a gradual variation in frequency is observed. During this initial period, the significant variation in the frequency correspond to a sudden decrease in the wave amplitude and a discontinuity in the instantaneous phase. These points are highlighted by vertical (dashed) lines in Fig. 3 and correspond to the splitting or merging of wavefronts in the image data. Such events and the observed discontinuities in the instantaneous phase have previously been associated with the appearance of topological defects [36]. Additionally, since wavenumber is not conserved at these bifurcation points where wavefronts are added or removed from the system, it is not surprising that multiple frequencies are observed in periodogram. This bifurcation that is observed in the frequency spectrum during the merging of two wavefronts is, however, an interesting observation. Further, it is observed that, over the duration of the data seen here, the mean frequency that is

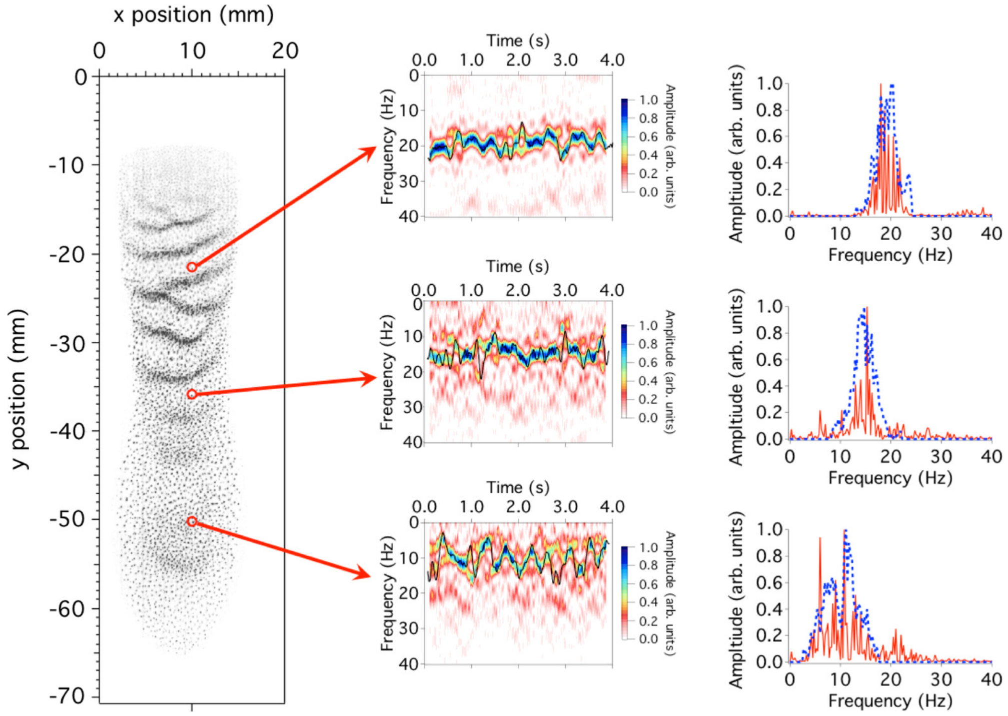

FIG. 4. (Color online) Comparison of the time-resolved Hilbert transform and the Fourier transform at the three spatial locations indicated in the image of the dust cloud in the left column. The middle column compares the time-resolved Hilbert transform (solid, black curve) to the frequency found by performing a short-time Fourier transform on the measured wave structure over the entire measurement sequence, while the right column depicts the distribution of the the mean frequencies found from the application of the time-resolved Hilbert transform (dashed, blue curve) and the Fourier spectra found by applying the Fourier transform to the wave structure over the entire measurement sequence (solid, red curve).

found through the use of this time-resolved Hilbert transform technique follows the dominant frequency in the system. Consequently, the mean frequency that is found here provides a temporally resolved measurement of the dominant frequency in the system.

A comparison of the mean frequency that is found from the application of this time-resolved Hilbert Transform technique with what is found using the Fourier Transform on the measured wave structure at three spatial locations located at different distances from the anode over the entire measurement sequence at $p = 91$ mTorr is seen in Fig. 4. In the first comparison, the mean frequency from the time-resolved Hilbert Transform is compared to the frequency found by performing a short-time Fourier Transform on the measured wave structure over the entire measurement sequence. This is seen in the middle column of Fig. 4. Here, it is observed that the mean frequency found through the application of the short-time Hilbert transform follows the dominant frequency seen in the periodogram constructed from the Fourier spectra found through the application of the short-time Fourier transform. Additionally, it is observed that the frequency generally decreases with increasing distance from the anode (i.e., the source of ions that drive the wave mode), a result that is consistent with previous measurements on this and other experimental devices [23,36]. In a second comparison, the distribution of the mean frequencies found using the time resolved Hilbert transform is compared to the Fourier spectrum that is found by applying the Fourier transform to the wave structure over the duration of the measurement sequence. This is seen in the right column of Fig. 4. Given the nature of the Hilbert transform, the distribution of mean frequencies should replicate the Fourier transform in the long-time limit (e.g., the Fourier spectra found when applying the Fourier transform to the entire measurement sequence). Excellent agreement is observed. Further, the general decrease in the wave frequency with increasing distance from the anode that was previously noted is clearly seen by the shift in the spectra toward lower frequencies. Taken together, this gives us confidence in the use of the time-resolved Hilbert transform technique to obtain spatiotemporal resolution of the evolution of the dominant frequency in the wave mode.

To extract the spatiotemporal properties of this wave mode, this time-resolved Hilbert transform technique is then carried out at every pixel location in the acquired image. A representative result at one time step, t_1, is seen in Fig. 5. From this, there are a few notable observations. First, a comparison of Figs. 5(a) and 5(b) shows that the phase, $\phi(x,y,t_1)$, does an excellent job of reproducing the wave structure, $n_d(x,y,t_1)$. Additionally, we observe abrupt changes in the phase at locations where wavefronts are observed to merge or split, a characteristic feature of a topological defect. Second, the frequency that is observed varies significantly over the acquired image and generally decreases with increasing distance from the anode (e.g., in the direction of decreasing y), which acts as the source of ions that drives the instability. Finally, one observes the existence of frequency clusters, which are more clearly seen by the superimposed contours

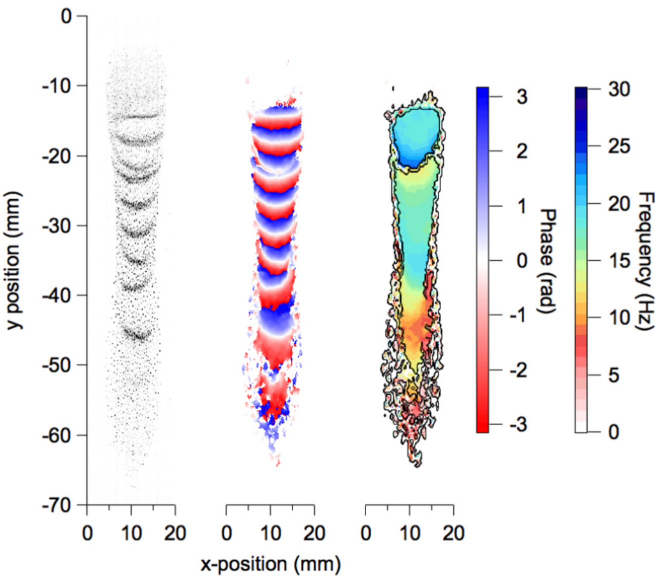

FIG. 5. (Color online) Plot showing (a) an inverted image of the dust cloud, (b) the instantaneous phase, and (c) the spatial distribution of frequency at a single time step with $p = 102$ mTorr. The phase and frequency plots have been filtered to only show points where wave activity was observed. Contours showing where the standard deviation in a 5×5 pixel region exceed 1 Hz are superimposed on the spatial distribution of frequency and serve as an indication of a boundary between frequency clusters. Movies showing the time evolution of this system at different pressures are available in the Supplemental Material [41].

that denote the standard deviation of the mean frequency over a 5×5 pixel box. Each of these observations are consistent with previously reported observations [32,36].

III. DISCUSSION

The spatial distribution of the wave structure, instantaneous phase, and mean frequency at a single instant in time are seen in Fig. 5. Of particular interest are the existence of frequency clusters, which are indicated by significant variations in the mean frequency and clearly identified by the superimposed contours that indicated the standard deviation of the spatial distribution of frequency over a 5×5 pixel region in Fig. 5(c). A more careful examination of these contours indicate that they occur at the merging or splitting of wavefronts due to differences in the speed at which the wavefronts propagate through the dust cloud. Movies showing the spatiotemporal evolution of the wave structure, instantaneous phase, and mean frequency at the three neutral pressures examined here can be viewed online; see Ref. [41].

A closer examination of the spatiotemporal properties of this wave mode reveal that the frequency clusters observed here are created by two distinct physical processes. In the first process, different regions of an individual wavefront are observed to propagate at different speeds leading to the merging or splitting of wavefronts. A time sequence of images and the spatial distribution of frequency depicting this process at $p = 91$ mTorr is seen in the left column of Fig. 6. Here, the arrows to the right of each plot highlights the propagation of a bifurcation in a wavefront as it propagates through the dust cloud. In this case, one observes a zipper-like process as the bifurcation is observed to traverse the leading wavefront, moving in the $+x$ direction, as the wavefronts propagate in the $-y$ direction. At the location of the bifurcation, there is a significant variation in the mean frequency, indicated by the linelike contours seen in Fig. 6, that propagate with the bifurcation in the wavefront. In the second case, individual wavefronts are observed to travel with a single phase velocity but the variation in the phase velocity of different wavefronts (see Table I) leads to two wavefronts merging as one wavefront overtakes a second wavefront as the two wavefronts propagate through the dust cloud. A time sequence of images and the spatial distribution of frequency depicting this process at $p = 102$ mTorr is seen in the right column of Fig. 6. Here, the black arrows to the left of each plot are used to highlight the merging of two wavefronts and the subsequent propagation of the resulting wavefront. In this case, one observes the formation of closed regions of distinct frequency at the spatial location where the two wavefronts merge, which is notably different than what is observed in the other process described. This situation is

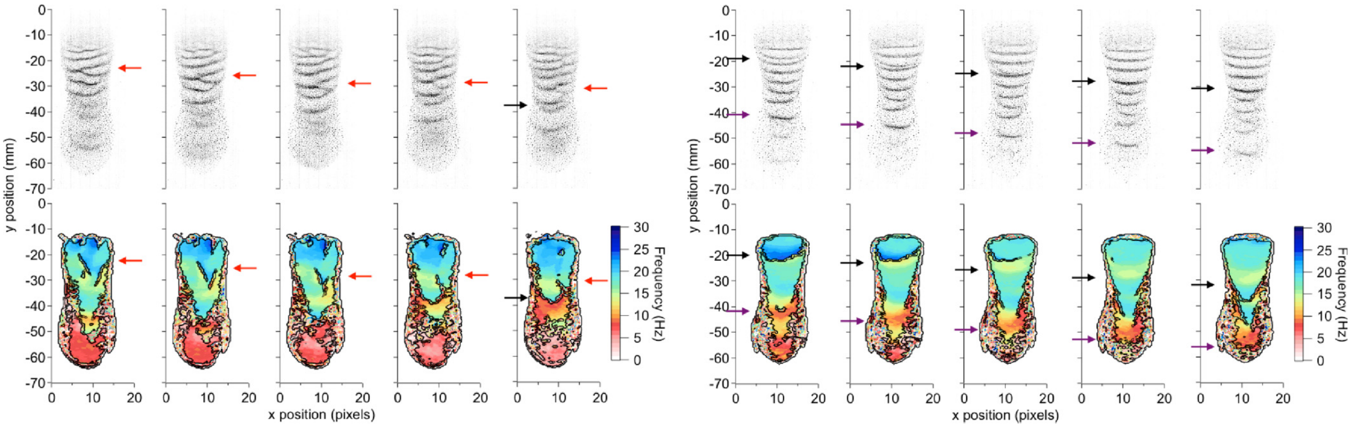

FIG. 6. (Color online) Image sequences showing the temporal evolution of the (top row) wave structure and (bottom row) spatial distribution frequency at $p = 91$ mTorr (left column) and 102 mTorr (right column). Contours depicting where the standard deviation in a 5×5 pixel region exceed 1 Hz are superimposed on the spatial distribution of frequency, which has been filtered to only show regions where there is significant wave activity. Arrows have also been added to highlight the propagation of particular wavefronts. The time between images is 40 ms.

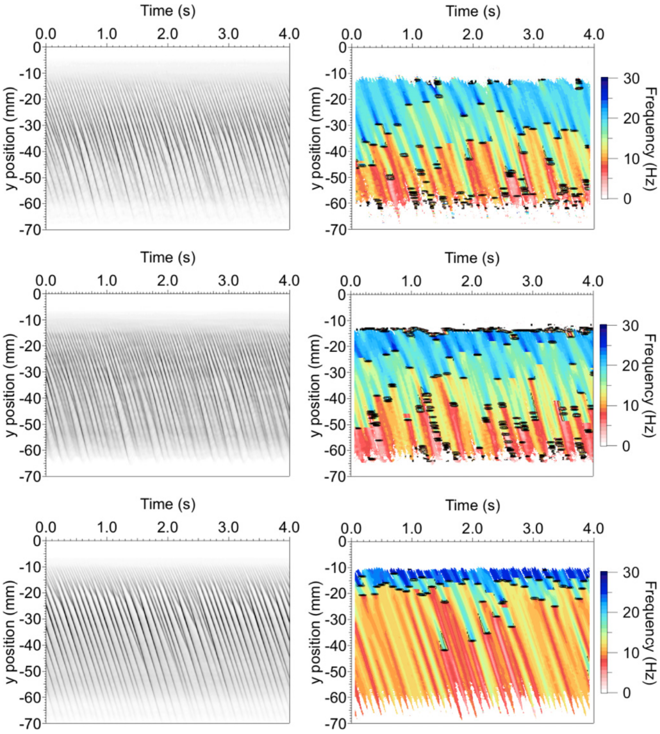

FIG. 7. (Color online) Space-time plots constructed by extracting a slice of the (left column) acquired image and (right column) spatial distribution of frequency from the center of the dust cloud at $p = 91$ mTorr (top row), 102 mTorr (middle row), and 118 mTorr (bottom row). Contours depicting where the standard deviation in a 5×5 pixel region exceed 1 Hz are superimposed on the space-time plots in the right column, which has been filtered to only show regions where there is significant wave activity.

also observed at $p = 91$ mTorr and is highlighted by the black arrow to the left of the plots seen in the left column of Fig. 6. It is noted that both of the processes described are observed to occur at each of the neutral pressures examined here.

In both cases, this merging or splitting of wavefronts leads to the injection of volumes of significantly different frequency that are observed to propagate with the merged or split wavefront, as highlighted by arrows in Figs. 6(c) and 6(d). This is more clearly seen in Fig. 7, where space-time plots are constructed by extracting vertical profiles from the center of the (left column) image and (right column) spatial distribution of frequency at $p = 91$ mTorr (top row), 102 mTorr (middle row), and 118 mTorr (bottom row). The contours that are superimposed on the space-time plots depicting the mean frequency (right column) indicate regions of significant variation in the spatial distribution of frequency and the existence of frequency clusters. Here, the use of a time-resolved Hilbert transform reveal that the frequency clusters exists for a short duration of time. Additionally, by comparing space-time plots from the image and frequency data, it is clear that the significant variation in the frequency that are associated with frequency clusters correspond the the merging and splitting of wavefronts. In addition to being localized in time, these frequency clusters are also observed to be spatially localized and that the spatial distribution of the frequency clusters becomes more localized as the neutral gas pressure increases. Finally, it is observed that there is a significant decrease in the frequency across these frequency clusters and that the lower frequencies that are observed after the frequency clusters then propagates with the merged or split wavefront until either another frequency cluster or the bottom edge of the cloud is reached.

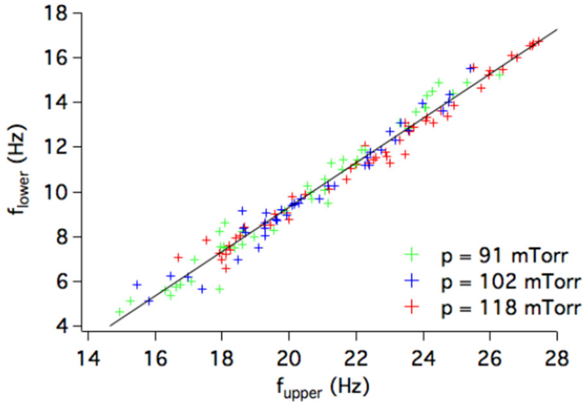

FIG. 8. (Color online) Plot of the frequency after a frequency cluster, f_{lower}, as a function of the frequency before a frequency cluster, f_{upper}, at the different neutral gas pressures examined. A linear fit (black curve) applied to all of the measured frequency pairs indicates that the frequency drops by ~10 Hz across these frequency clusters independent of the experimental parameters.

It is possible to compare the frequency above, f_{upper}, and below, f_{lower}, the frequency clusters that are observed in the right column of Fig. 7. This is seen in Fig. 8, where the frequency pairs from opposing sides of these bifurcation points or frequency clusters are plotted. A linear fit to all of the data over the range of neutral pressures examined here reveal that for this set of experimental conditions, the frequency is observed to drop by ~10 Hz at the interface between frequency clusters. Qualitatively, this result is similar to what has been observed in pervious experimental studies [36] and in numerical simulations [37], suggesting that this may be understood in the context of modeling this system an ensemble of coupled van der Pol oscillators.

IV. CONCLUSIONS

To summarize, we have applied a short-time Hilbert transform technique to analyze the spatiotemporal evolution of the naturally occurring dust acoustic wave over a range of neutral gas pressures. Frequency clusters were observed to exists for short periods of time over the range of pressures examined and became concentrated in more localized spatial regions of the cloud as the pressure was increased. Additionally, it was observed that the frequency dropped by ~10 Hz across these frequency clusters independent of the neutral gas pressure or spatial location of the frequency cluster.

ACKNOWLEDGMENTS

This work is supported by the US National Science Foundation through Grant No. PHY-0953595. We thank Professor Alexander Piel from the Christian-Albrechts-Universität for suggesting the use of the Hilbert transform technique.

[1] N. D'Angelo, Planet. Space Sci. **38**, 1143 (1990).
[2] P. K. Shukla, Plasma Phys. Control. Fusion **42**, B213 (2000).
[3] M. Rosenberg, Astrophys. Space Sci. **277**, 125 (2001).
[4] P. K. Shukla and B. Eliasson, Rev. Mod. Phys. **81**, 25 (2009).
[5] E. Thomas, Jr., Contr. Plasma Phys. **49**, 316 (2009).
[6] N. N. Rao, P. K. Shukla, and M. Y. Yu, Planet. Space Sci. **38**, 543 (1990).
[7] A. Barkan, R. L. Merlino, and N. D'Angelo, Phys. Plasmas **2**, 3563 (1995).
[8] F. Verheest, *Waves in Dusty Space Plasmas* (Kluwer Academic Press, Norwell, MA, 2000).
[9] P. K. Shukla and A. A. Mamun, *Introduction to Dusty Plasma Physics* (Institute of Physics Publishing, Bristol, England, 2002).
[10] S. V. Vladimirov, K. Ostrikov, and A. A. Samarian, *Physics and Applications of Complex Plasmas* (Imperial College Press, London, 2005).
[11] A. Piel, *Plasma Physics: An Introduction to Laboratory, Space, and Fusion Plasmas* (Springer-Verlag, Berlin, 2010).
[12] R. L. Merlino, Phys. Plasmas **16**, 124501 (2009).
[13] M. Schwabe, M. Rubin-Zuzic, S. Zhdanov, H. M. Thomas, and G. E. Morfill, Phys. Rev. Lett. **99**, 095002 (2007).
[14] C.-T. Liao, L.-W. Teng, C.-Y. Tsai, C.-W. Io, and L. I, Phys. Rev. Lett. **100**, 185004 (2008).
[15] M. Schwabe, S. K. Zhdanov, H. M. Thomas, A. V. Ivlev, M. Rubin-Zuzic, G. E. Mor fill, V. I. Molotkov, A. M. Lipaev, V. E. Fortov, and T. Reiter, New J. Phys. **10**, 033037 (2008).
[16] E. Thomas, Jr., Phys. Plasmas **13**, 042107 (2006).
[17] T. M. Flanagan and J. Goree, Phys. Plasmas **17**, 123702 (2010).
[18] T. M. Flanagan and J. Goree, Phys. Plasmas **18**, 013705 (2011).
[19] J. D. Williams, IEEE Trans. Plasma Sci. **41**, 788 (2013).
[20] T. Trottenberg, D. Block, and A. Piel, Phys. Plasmas **13**, 042105 (2006).
[21] E. Thomas, Jr., R. Fisher, and R. L. Merlino, Phys. Plasmas **14**, 123701 (2007).
[22] J. D. Williams, E. Thomas, Jr., and L. Marcus, Phys. Plasmas **15**, 043704 (2008).
[23] I. Pilch, T. Reichstein, and A. Piel, Phys. Plasmas **16**, 123709 (2009).
[24] V. Nosenko, S. K. Zhdanov, S. H. Kim, J. Heinrich, R. L. Merlino, and G. E. Morfill, Europhys. Letters **88**, 65001 (2009).
[25] E. Thomas, Jr., Phys. Plasmas **17**, 043701 (2010).
[26] L.-W. Teng, M.-C. Chang, Y.-P. Tseng, and L. I, Phys. Rev. Lett. **103**, 245005 (2009).
[27] P. K. Shukla and Lin I, Phys. Lett. A **374**, 1165 (2010).
[28] J. Heinrich, S.-H. Kim, and R. L. Merlino, Phys. Rev. Lett. **103**, 115002 (2009).
[29] R. L. Merlino, J. R. Heinrich, S. H. Hyun, and J. K. Meyer, Phys. Plasmas **19**, 057301 (2012).
[30] C. Thompson, A. Barkan, N. D'Angelo, and R. L. Merlino, Phys. Plasmas **4**, 2331 (1997).
[31] J. D. Williams and J. Duff, Phys. Plasmas **17**, 033702 (2010).
[32] K. O. Menzel, O. Arp, and A. Piel, Phys. Rev. Lett. **104**, 235002 (2010).
[33] W. D. Suranga Ruhunusiri and J. Goree, Phys. Rev. E **85**, 046401 (2012).
[34] J. Pramanik, B. M. Veeresha, G. Prasad, A. Sen, and P. K. Kaw, Phys. Lett. A **312**, 84 (2003).
[35] Y.-Y. Tsai, M.-C. Chang, and L. I, Phys. Rev. E **86**, 045402(R) (2012).
[36] K. O. Menzel, O. Arp, and A. Piel, Phys. Rev. E **83**, 016402 (2011).
[37] K. O. Menzel, O. Arp, and A. Piel, Phys. Rev. E **84**, 016405 (2011).
[38] J. D. Williams and E. Snipes, IEEE Trans. Plasma Sci. **38**, 847 (2010).
[39] M. Lampe, R. Goswami, Z. Sternovsky, S. Robertson, V. Gavrishchaka, G. Ganguli, and G. Joyce, Phys. Plasmas **10**, 1500 (2003).
[40] S. A. Khrapak and G. E. Morfill, Phys. Plasmas **19**, 024510 (2012).
[41] See Supplemental Material at http://link.aps.org/supplemental/10.1103/PhysRevE.89.023105 for a movie that shows the spatiotemporal evolution of the wave at different neutral gas pressures.